Damage Quantification via Digital Volume Correlation with Heterogeneous Mechanical Regularization: Application to an In Situ Meso-Flexural Test on Mortar

Aliaksandra Tsitova, Fabien Bernachy-Barbe, Benoît Bary, Sirine Al Dandachli, Christophe Bourcier, Benjamin Smaniotto, François Hild

Experimental Mechanics manuscript No.
(will be inserted by the editor)

Damage Quantification via Digital Volume Correlation with Heterogeneous Mechanical Regularization: Application to an In Situ Meso-Flexural Test on Mortar

Aliaksandra Tsitova · Fabien Bernachy-Barbe · Benoît Bary · Sirine Al Dandachli · Christophe Bourcier · Benjamin Smaniotto · François Hild

Received: date / Accepted: date

Abstract Background. The mechanical response and damage mechanisms of heterogeneous cementitious materials result from the mechanical properties of their

A. Tsitova, F. Bernachy-Barbe (formerly), B. Bary, S. Al Dandachli
Université Paris-Saclay, CEA, Service d'Etude du Comportement des Radionucléides, 91191, Gif-sur-Yvette, France
C. Bourcier
Université Paris-Saclay, CEA, Service d'Etudes Mécaniques et Thermiques, 91191, Gif-sur-Yvette, France
A. Tsitova, B. Smaniotto, F. Hild
Université Paris-Saclay, ENS Paris-Saclay, CNRS
LMT - Laboratoire de Mécanique et Technologie, 91190 Gif-sur-Yvette, France
Corresponding author. E-mail: francois.hild@ens-paris-saclay.fr
F. Bernachy-Barbe
CEA, DES, IRESNE, DEC, Cadarache, 13108 Saint-Paul-lez-Durance, France

constituents at the mesoscale. Objective. In this study, a finite element based Digital Volume Correlation (FE-DVC) method with mechanical regularization tailored for heterogeneous materials was applied to study crack propagation in mortar. Method. A realistic 3D mesh was built consistently with the actual microstructure based on high resolution X-ray tomography. A notched mesobeam was subjected to *in situ* three-point flexure. Results. The introduction of mechanical contrast in DVC analyses allowed the strain heterogeneities related to the underlying microstructure to be described and inelastic strain localization due to cracks to be captured. Furthermore, the relaxation of mechanical regularization in damaged elements improved the trustworthiness of displacement measurements. Conclusion. Estimations of crack opening displacements and characterization of the crack morphology were carried out, providing insights into the damage processes at the mesoscale.

Keywords Digital Volume Correlation (DVC) · X-Ray tomography · Three-point flexural test · Microscale · Mechanical regularization

1 Introduction

X-ray Computed Tomography (XCT) has become a powerful tool for the acquisition of 3D images and is widely used in material science [1]. Static 3D images are being utilized for morphological and quantitative microstructure characterization that can be considered for image-based numerical modeling [2,3]. Tomographic studies have found numerous applications for cementitious materials due to their high heterogeneity and complex compositions. One example among various applications is the microstructure characterization based on X-ray imaging. Studies

were carried out on aggregate and cement particle shapes [4–9], pore and crack networks [5, 10–15], and cement paste morphology [16, 12]. Such studies allowed for example estimations of concrete permeability and hydration processes. Moreover, X-Ray based microstructures were used for mechanical and thermal property estimations [17], as input to finite element (FE) models [18–20] and FFT-based simulations [21].

Beyond static imaging, the continuation of these studies was the observation of microstructural changes due to exposure to aggressive environments or thermo-hydro-mechanical loadings. Taking sequences of 3D images under different environmental conditions allowed the microstructure changes to be tracked. Tomographic studies were reported on cementitious materials subjected to leaching [22, 23], sulfate attacks [24], corrosion [25], and water migration [26]. One of the extensions to this technique is *in situ* testing when experiments are carried out inside CT scanners [27]. Registering 3D scans allows different deformation mechanisms such as damage growth, crack opening, or shear banding to be quantified as a function of time or mechanical loading. In particular, it allowed complex damage processes to be visualized in concrete. The characterization of damage growth with X-CT scanning was carried out under mechanical [20, 28–31] and hydrostatic *in situ* loadings [32], subjected to freezing-thawing cycles [33] or autogeneous shrinkage [34].

Apart from image analyses and processing, Digital Volume Correlation (DVC) became a popular technique to measure three-dimensional displacement and strain fields with subvoxel resolution [35, 36]. DVC appeared as an extension of Digital Image Correlation (DIC) that was developed for 2D images [37]. The principle of these methods first consisted in measuring displacements of small subvolumes registered between reference and deformed volumes. Later on, finite element ap-

proaches were introduced [38]; the registrations are performed at the level of the whole region of interest. DVC analyses were performed for concrete subjected to *in situ* mechanical loadings [43,42,39–41], hydrothermal loadings [44], carbonation [45] and reinforcement corrosion [46]. The study of damage development was possible by analyzing displacement or strain fields as they normally indicate crack locations [47] respectively as discontinuities or high values. Another way of displaying crack networks was via residual fields, which are the difference images between the reference volume and the deformed volume corrected with the measured displacement field [48,49,47,50].

In the present study, an FE-DVC method with mechanical regularization tailored for heterogeneous materials was used to quantify damage in mortar. Mechanical regularization was initially introduced in a homogeneous setting for DVC analyses [51,52]. Then, it was adapted to heterogeneous materials in a DIC framework [53] by taking into account the contrast in elastic properties of different phases. Damage was also added to allow localized solutions to be retrieved [47]. In the present case, a mesh was built consistently with the underlying microstructure, based on an X-ray microtomography scan acquired prior to the *in situ* test. Then, a notched microbeam was subjected to *in situ* three-point flexure. In order to image a larger part of the beam, a lower resolution was selected. The realistic volume mesh was backtracked via DVC from the high resolution scan to the *in situ* scan. The influence of mechanical contrast on the trustworthiness of 3D displacement and strain fields was studied. Furthermore, the damaged elements were detected in order to take into account their reduced stiffness in mechanical regularization. This technique allowed the displacement measurements to be consistent in the

damaged areas. The final DVC results were used for crack opening estimations and a study of the crack morphology at the mesoscale.

The study workflow (Figure 1) summarizes the different steps of the present study, whose aim is to demonstrate the potential of mechanically regularized DVC based on the underlying microstructure for the study of damage at low scales.

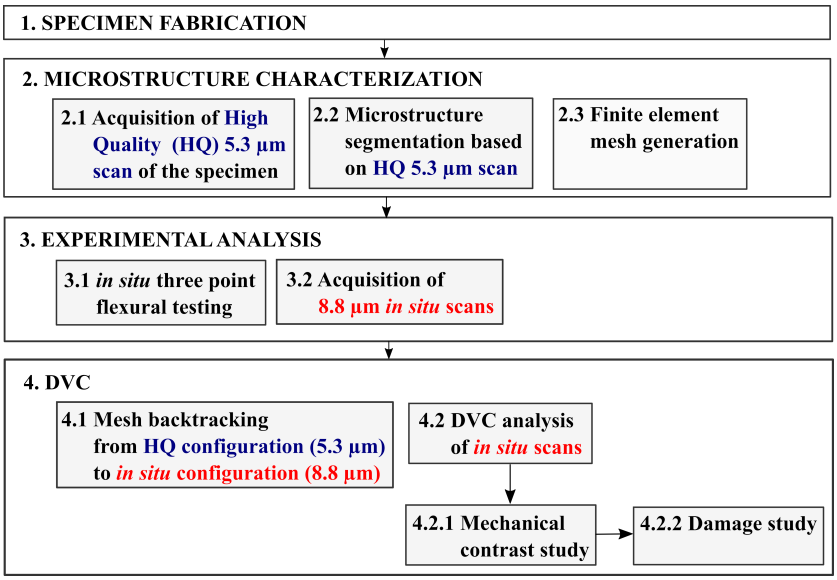

Fig. 1 Experimental and numerical workflow

2 Material and Methods

This section describes the specimen fabrication process and provides a description of the microstructure characterization procedure that was used to reconstruct a realistic 3D mesh. The experimental setup and protocol are then detailed. The section ends with a description of heterogeneous regularization within an FE-DVC framework.

2.1 Material and Specimen

A mortar batch was mixed using a CEM I Portland cement with a water-to-cement ratio of 0.525. A low sand-to-binder ratio was used (0.5). Sand was sieved to obtain a granulometric distribution within the range 200 µm to 2 mm in diameter. The reduction of the sand volume fraction to 18%, and elimination of fine particles, made the resulting microstructure more suitable for efficient image processing as less geometric details were distorted or lost. A thin mortar plate with dimensions $65 \times 35 \times 8$ mm was cast in a silicon mold and unmolded after 1 day. By means of X-ray radiography, the mortar plate was checked for the absence of mesocracking and defects. After control, the plate was selected for further fabrication.

First, the top surface was ground and polished until a 5 mm thickness was reached with simultaneous control of parallelism of the top and bottom faces. The thickness deviation was of the order 0.1 mm, which corresponds to a $\angle 1.5‰$ inclination between the top and bottom surfaces. Second, the plate width was adjusted to 20 mm with a wire saw. Third, $5 \times 5 \times 20$ mm microbeams (Figure 2) were cut from the plate with a diamond disk saw to ensure planar parallel sides. Fourth, the notch was cut with a saw equipped with a fine (0.1 mm) wire and low tension to avoid sample degradation. The notch width was approximately 0.15 mm and its height was 1.5 mm. The specimen were stored at 100% air humidity. During preparation, the specimen surfaces were re-wetted to prevent them from drying cracking.

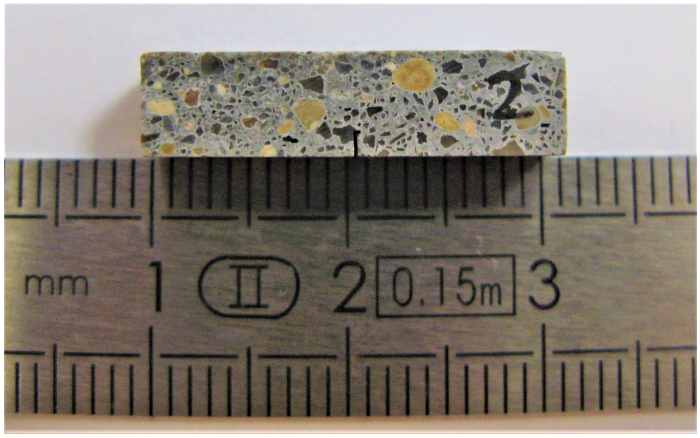

Fig. 2 Notched mortar microbeam

2.2 Microstructure Segmentation and Microstructure-Based Mesh

Before the *in situ* test, a High Quality (HQ) scan of the central part of the microbeam was acquired with a 5.3 µm resolution using a GE Phoenix v|tome|x m CT system. The acquisition parameters are detailed in Table 1.

Table 1 DVC hardware parameters

Parameters	High Quality Scan	*In situ* Scan
CT device	GE Phoenix v|tome|x M	
Target	high-flux|target	
Filter	0.1 mm Cu	
Voltage	180 kV	200 kV
Current	57 µA	90 µA
Tube to detector	807.3 mm	
Tube to object	21.5 mm	35.5 mm
Detector	GE Dynamic 41|100	
Definition	1992×2000 (2×2 binning)	
Number of projections	2500	1600
Angular amplitude	360°	
Frame average	5 per projection	3 per projection
Frame rate	2 fps	3 fps
Acquisition duration	2.5 h	45 min
Gray Level amplitude	14 bit (16 bit format)	
Pixel size	5.3 µm	8.8 µm

Avizo® data visualization and analysis software was used for further image processing. After mechanical testing (Section 2.3), a Region Of Interest (ROI) containing the notch with dimensions $2.6 \times 5 \times 5$ mm was selected for further segmentation (Figure 6). First, a median filter ($3 \times 3 \times 3$ voxels) was applied to mitigate noise (Figure 3(a)).

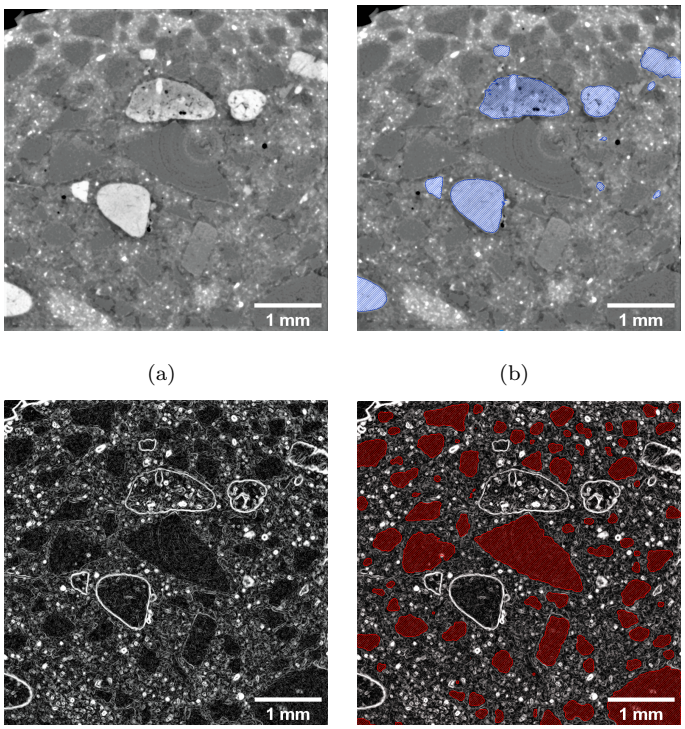

Fig. 3 Inclusion segmentation. (a) Filtered image (light inclusions - limestone aggregates, gray inclusions - siliceous aggregates). (b) Segmentation of limestone aggregates. (c) Contrast (norm of image gradient). (d) Segmentation of siliceous particles

Second, the segmentation of aggregates was carried out as follows. Two types of inclusions (limestone – $CaCO_3$, silica – SiO_2) were present in mortar with different morphology and levels of attenuation that define their representation on images. Limestone inclusions were brighter (higher X-ray absorption) than the cementitious matrix, and were separated by simple thresholding (Figure 3(b)). Silica inclusions had similar gray levels as the cement paste matrix, but showed less internal contrast and appeared as very homogeneous regions. The calculation of the image gradient norm gave a field with low values in homogeneous zones, and high

levels in heterogeneous regions (Figure 3(c)). This tool allowed the homogeneous inclusions to be distinguished from the heterogeneous matrix (Figure 3(d)). These two families of inclusions were considered as a unique "aggregate" phase with identical elastic properties. Mesoporosity was present in the specimen in a small amount, and did not seem to have a major effect on the crack path during the flexural test. For these reasons, mesopores were not segmented as a separate phase and were incorporated in the matrix. Last, the notch surfaces were segmented from the volume (Figure 4(a)).

Based on the segmentation results, the Avizo® tools allowed surface triangular meshes to be generated and exported in .stl format. The size of surface triangles was controlled to be at least several voxels for consistency with DVC, and with simultaneous check of excessive distortion of triangles. The surface meshes were then processed with the tools available in the Salome® platform (https://www.salome-platform.org/) to obtain 4-noded tetrahedral elements (Figure 4(b,c)). The mesh consisted of 346,472 tetrahedra and 63,465 nodes. The distribution of mesh elements and volume between the different phases is given in Table 2.

Table 2 Characteristics of the phases in the mesh. The physical size of one voxel is 8.8 µm

	Aggregates	Matrix	Interphase	Bulk matrix
Elements	74,120	272,352	134,474	137,878
Nodes	7,863	-	16,232	39,279
Volume, vx^3	$1.57 \cdot 10^7$	$5.50 \cdot 10^7$	$2.61 \cdot 10^7$	$2.89 \cdot 10^7$
Volume fraction	22%	78%	37%	41%
Element size, vx	6	6	6	6
Young's modulus, GPa	70.0	13.3	13.3	13.3
Poisson's ratio	0.26	0.26	0.26	0.26

In the matrix, elements adjacent to aggregates are denoted as interphase elements, and the remainder of the matrix are bulk elements. The equivalent element size, which is defined as the cubic root of the volume of each element, was equal on average to 10 vx (or 53 µm) in the HQ configuration and 6 vx in the LQ setting (Table 2). The mesh fineness was identical in the matrix and the aggregates.

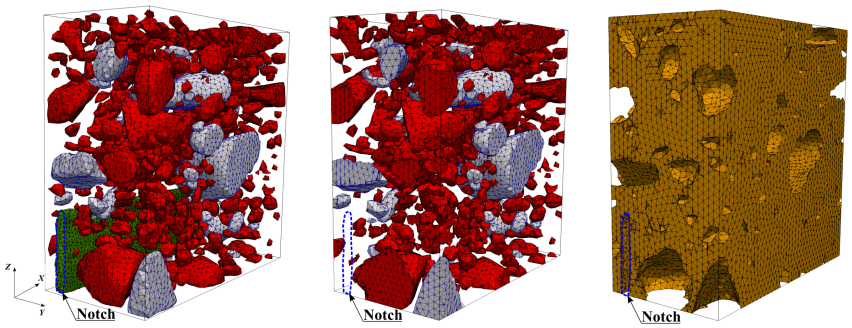

(a) (b) (c)

Fig. 4 Surface and volume meshes (red: siliceous aggregates, gray: limestone aggregates, yellow: matrix, green: notch). (a) Surface meshes. (b) Aggregate and (c) matrix meshes

2.3 Experimental Analysis

The *in situ* flexural test was performed with the LMT *in situ* Tension-Compression (TC) testing machine designed at the MATEIS laboratory [27]. The load capacity is ±1 kN. Tensile or compressive loads can be applied by axial displacement of the bottom actuator. The adapted setup for three-point flexural tests is shown in Figure 5. The vertical motion of the bottom actuator with part A1 causes a horizontal motion of support parts B and C thanks to 45° contact surfaces. The shortening of the distance between B and C results in point load application to the sample that is equivalent to three-point flexure. The parts of the flexural setup

were manufactured in an aluminium alloy as it has a high stiffness and reasonable X-ray attenuation compared to mortar, which allowed additional artifacts to be avoided. Thin adhesive tape was attached to the top and bottom faces of the beam for maintaining the sample and improving its stability during testing. The adhesive tape was also used for fastening the parts of the setup to ensure better control over sample positioning inside it, and for safe insertion of the setup into the tube of the TC machine.

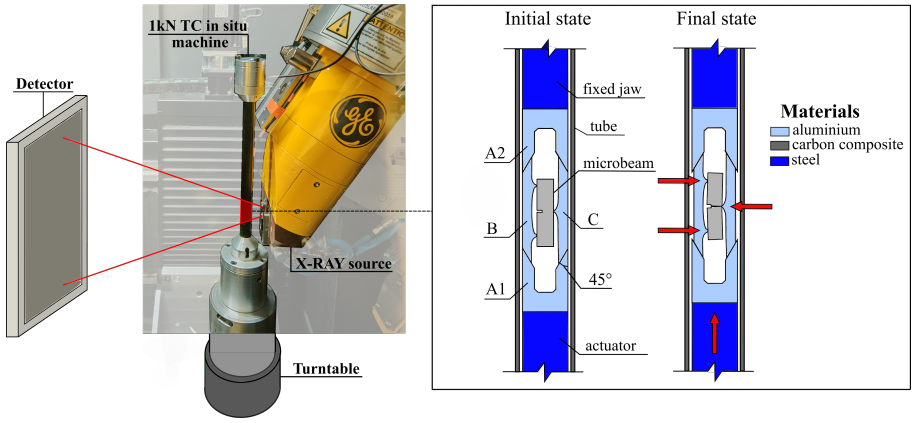

Fig. 5 Schematic and actual views of the *in situ* three-point flexural setup

The *in situ* test consisted of several loading steps, and CT scans were performed at sustained and constant load. The experimental protocol and load levels of CT scans are shown in Figure 6(a). The scans were acquired with the Phoenix v|tome|x m scanner (Table 1). First, two successive scans were performed on the undeformed specimen for uncertainty quantification. A small preload of 1 N was applied to keep the specimen stable. Second, axial displacements were applied with 0.5 µm/s rate until sample failure. The experimental configuration along with the specimen geometry did not allow for a fine control of crack initiation and propa-

gation. Failure was brittle, followed by substantial force drop, and very fast crack propagation on the major part of the ligament (Figure 6(b)). The second scan was carried out immediately after fracture. Third, an increment of axial displacement of 20 textmum was applied to further open the crack. After each loading, a 10 min dwell was applied before the next scan (*i.e.,* force relaxation was stabilized).

In the reported test, the loading point was not fully aligned with the notch. This off-axis loading resulted in a bifurcation of the fractured surface into two main cracks (Figure 6(b)). The Region of Interest (ROI) was chosen to encompass all fractured surfaces while maintaining a small gap with an irregular external surface. They were observed to cross the cement paste matrix, aggregate-matrix interfaces and limestone aggregates.

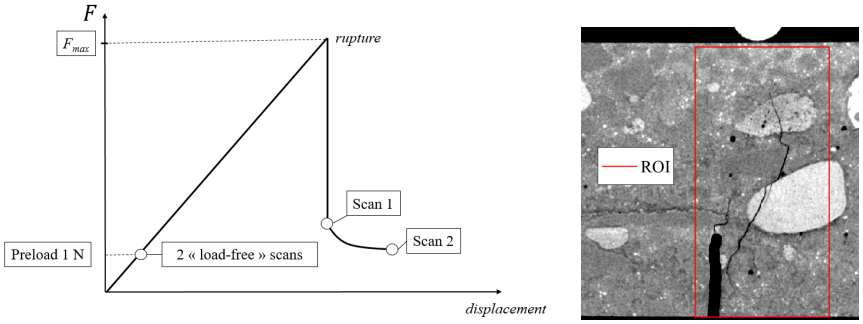

(a) (b)

Fig. 6 (a) CT scans performed during *in situ* flexure. (b) 2D section of fractured specimen and DVC ROI

2.4 Regularized DVC for Heterogeneous Materials

DVC measures displacement fields in the selected ROI by registering the deformed volumes g and the reference volume f assuming gray level conservation

$$f(\mathbf{x}) = g(\mathbf{x} + \mathbf{u}(\mathbf{x})) \tag{1}$$

where $\mathbf{u}(\mathbf{x})$ is the sought displacement field, and $\mathbf{x}$ any voxel position within the ROI. The sought displacement field has to minimize the gap to gray level conservation

$$\min_{\{\mathbf{u}\}} \Phi_c^2 = \sum_{\text{ROI}} [f(\mathbf{x}) - g(\mathbf{x} + \mathbf{u}(\mathbf{x}))]^2 \tag{2}$$

with

$$\mathbf{u}(\mathbf{x}) = \sum_n u_n \boldsymbol{\phi}_n(\mathbf{x}) \tag{3}$$

where $\boldsymbol{\phi}_n(\mathbf{x})$ are trial displacement fields, and u_n the associated Degrees Of Freedom (DOFs) gathered in the column vector $\{\mathbf{u}\}$. In FE-DVC, the sought DOFs are the nodal displacements of a finite element discretization, and $\boldsymbol{\phi}_n(\mathbf{x})$ the corresponding shape functions.

The minimization of Equation (2) is equivalent to iteratively solving a sequence of linear systems [54]

$$[\mathbf{M}]\{\delta\mathbf{u}\} = \{\mathbf{b}\} \tag{4}$$

where $[\mathbf{M}]$ is the DVC Hessian matrix, whose terms are products of the shape functions by the gradient of the reference volume, $\{\mathbf{b}\}$ the residual vector, which is a function of the difference between the reference and the corrected deformed volumes, and $\{\delta\mathbf{u}\}$ the corrections to the current estimate of the nodal displacement vector $\{\tilde{\mathbf{u}}\}$.

198 The gray level residual field $\varphi_c = f(\mathbf{x}) - g(\mathbf{x} + \mathbf{u}(\mathbf{x}))$ represents the difference
199 between the volume in the reference configuration and that in the deformed con-
200 figuration corrected by the measured displacement field. The global residual Φ_c,
201 which is to be minimized, is the root mean square (RMS) of the residual field φ_c
202 and serves as indicator of the consistency of the solution, namely, a smaller RMS
203 residual means a more trustworthy solution. Local high residual values may mark,
204 for example, discontinuities in displacements, or in other words, cracks [48, 49,
205 47]. Last, it is worth noting that the residual fields are, by definition, Lagrangian
206 (*i.e.,* constructed in the reference configuration).

207 The correlation problem is ill-posed and the introduction of mechanical regu-
208 larization is one of the ways to make it well-posed [51, 55, 52]. In regularized DVC,
209 elasticity is enforced at a local level by the introduction of a penalty term based
210 on the equilibrium gap

$$[\mathbf{K}_1]\{\mathbf{u}\} = \{\mathbf{f}_r\} \tag{5}$$

211 where $[\mathbf{K}_1]$ is the rectangular stiffness matrix restricted to inner nodes and traction-
212 free surfaces, and $\{\mathbf{f}_r\}$ the nodal force vector that must vanish in the absence of
213 body forces. The mechanical penalty term is formulated as the $L2$-norm of the
214 force residuals

$$\Phi_m^2 = \{\mathbf{u}\}^\top [\mathbf{K}_1]^\top [\mathbf{K}_1]\{\mathbf{u}\} \tag{6}$$

215 For other boundary (*i.e.,* Dirichlet) nodes, the fluctuations of tractions are
216 regularized

$$\Phi_b^2 = \{\mathbf{u}\}^\top [\mathbf{K}_2]^\top [\mathbf{L}][\mathbf{K}_2]\{\mathbf{u}\} \tag{7}$$

217 where $[\mathbf{L}]$ is based upon the Laplace-Beltrami operator [56], and $[\mathbf{K}_2]$ the rectan-
218 gular stiffness matrix restricted to Dirichlet nodes. These additional cost functions

do not have the same physical units as Φ_c^2. Therefore, to minimize their weighted sum, they are normalized

$$\tilde{\Phi}_m^2 = \frac{\Phi_m^2}{\{\mathbf{v}\}^\top[\mathbf{K}]^\top[\mathbf{K}]\{\mathbf{v}\}}, \tilde{\Phi}_b^2 = \frac{\Phi_b^2}{\{\mathbf{v}\}^\top[\mathbf{L}]^T[\mathbf{L}]\{\mathbf{v}\}}, \tilde{\Phi}_c^2 = \frac{\Phi_c^2}{\{\mathbf{v}\}^\top[\mathbf{M}]\{\mathbf{v}\}} \tag{8}$$

where $\mathbf{v} = \mathbf{v}_0 \ \exp(i\mathbf{k}\cdot\mathbf{x})$ is the trial displacement field selected in the form of a plane wave, $\mathbf{v}_0$ the amplitude, and $\mathbf{k}$ the wave vector [51,55]. The global minimization is performed on the weighted sum of the normalized cost functions

$$(1 + w_m + w_b)\Phi_t^2 = \tilde{\Phi}_c^2 + w_m\tilde{\Phi}_m^2 + w_b\tilde{\Phi}_b^2 \tag{9}$$

where Φ_t is the total cost function. The weights w_m and w_b are defined as

$$w = w_m = w_b = (2\pi k\ell_{reg})^4 \tag{10}$$

where ℓ_{reg} is the regularization length, and $k = \|\mathbf{k}\|$ the wave number. Up to now, mechanical regularization was based upon homogeneous, isotropic and linear elasticity [51,52]. If ℓ_{reg} is greater than the element size, mechanically inadmissible displacement fluctuations are filtered out over a spatial domain of size proportional to ℓ_{reg}. In the case of damage or localized plastic strains, displacement discontinuities are smeared over a domain whose size that depends on ℓ_{reg} [52,47].

As the microstructure-based mesh differentiates matrix and aggregate elements (Figure 4(c)), the proposed regularization can take into account differences in elastic properties, as already performed in 2D DIC applied to a composite material [53]. For a two-phase material, the contrast C is introduced to denote the ratio of Young's moduli of the matrix E_m and the inclusions E_i

$$C = \frac{E_i}{E_m} = \sqrt{\frac{w^i}{w^m}} = \left(\frac{\ell_{reg}^i}{\ell_{reg}^m}\right)^2 \tag{11}$$

where w^i and w^m denote the weight in the inclusions and in the matrix, respectively. In such formulation, $C > 1$ implies that inclusions are more rigid than the matrix, and more weight is put on the inclusion phase. Conversely, $C < 1$ corresponds to inclusions being more compliant and a larger weight is put on the matrix phase. The case $C = 1$ is equivalent to homogeneous elastic regularization.

Mechanically regularized DVC was implemented within the Correli 3.0 framework developed at LMT [57]. Table 3 gathers the DVC parameters utilized in the following analyses. For the sake of simplicity, ℓ_{reg} also denotes the regularization length in the matrix phase (*i.e.,* ℓ^m_{reg}), if heterogeneous regularization is performed since in the present case, $C < 1$ is very unlikely.

Table 3 DVC analysis parameters

DVC software	Correli 3.0 [57]
Image filtering	none
Element length ℓ (mean)	6 vx (53 µm) in *in situ* configuration
Shape functions	linear (4-noded tetrahedra)
Mesh	see Figure 4(b,c)
Matching criterion	Penalized sum of squared differences (Equation (9))
Interpolant	cubic
Displacement noise floor	see Figure 8(a)
Strain noise floor	see Figure 8(b)

3 DVC Results and Discussion

This section describes the DVC analysis workflow that begins with the mesh backtracking procedure [58]. Then, a quantification of uncertainties for different values

of regularization length and contrasts was performed. Last, DVC analyses for different contrasts were carried out on the deformed (and damaged) volume.

3.1 Mesh Backtracking

The microstructure-based mesh was reconstructed on the HQ scan with a 5.3 µm/vx resolution acquired prior to the *in situ* test (see blue mesh in Figure 7). As mentioned above, the HQ and *in situ* (LQ) scans were acquired with different resolutions and acquisition parameters (Table 1). Before performing DVC analyses, the mesh had to be backtracked to take into account scale differences and rigid body motions between the two scans (*i.e.,* initially mispositioned blue mesh in the LQ configuration in Figure 7(left)). This step was important as if the mesh did not match accurately the underlying microstructure, heterogeneous regularization would be meaningless.

Backtracking consists in running a DVC analysis between the HQ scan (volume f in Equation (1)) and the *in situ* scan (volume g) of the undeformed specimen to find the displacement field $\mathbf{u}_b$ linking the two configurations [58]. In the present case, the HQ scan was binned to a resolution of 10.6 µm/vx, and both scans were converted into 8-bit volumes. An auxiliary mesh was used, consisting of a rectangular hexahedral mesh composed of large T4 elements (their size was 25 vx or 250 µm in the reference HQ configuration) that encompassed the volume of the microstructure-based mesh (*i.e.,* $4.5 \times 4.75 \times 2.3$ mm, see the magenta mesh depicted in Figure 7).

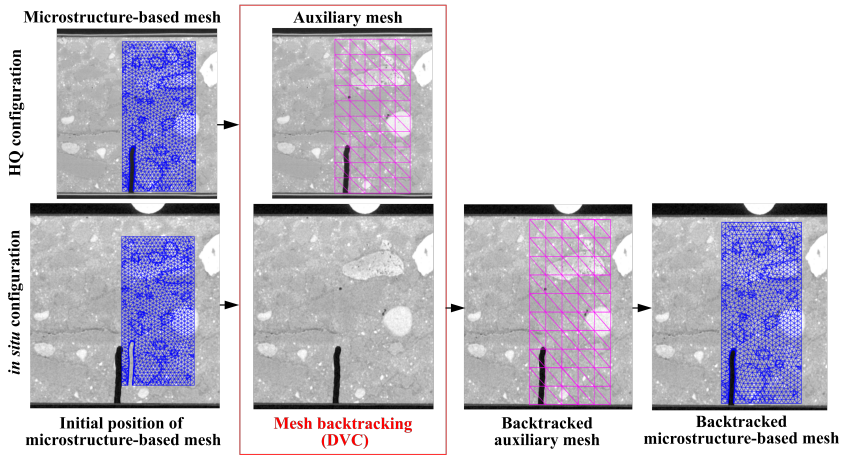

Fig. 7 Schematic view of the backtracking procedure enabling the (blue) mesh based on the HQ configuration (top) to be fitted to the *in situ* configuration (bottom) via DVC using an auxiliary (magenta)

mesh

The calculation was initialized with a displacement field containing scaling and rigid body degrees of freedom. After DVC convergence, the displacement field $\mathbf{u}_{aux}$ enabled the auxiliary mesh to be positioned in the LQ configuration. The interpolation of the displacement field $\mathbf{u}_{aux}$ at the nodes of the meshed microstructure yielded $\mathbf{u}_b$, which gave the nodal coordinate corrections to fit it back to the *in situ* (LQ) configuration (*i.e.*, repositioned blue mesh in the LQ configuration shown in Figure 7(right)).

3.2 Uncertainty Quantification

Uncertainty quantifications were performed by running DVC analyses on the two scans performed on the undeformed specimen. Four different contrasts were considered to investigate the effects of this parameter on the results. First, the contrast C

was set to 1, which implied that the elastic properties of the different phases were identical. This choice was equivalent to homogeneous mechanical regularization. Second, the contrast C was set to $E_i/E_m = 70.0/13.3 = 5.26$, which corresponds to realistic properties of mortar constituents when inclusions were more rigid that the cementitious matrix [59]. Third, the case $C = 0.5$ was considered, which implied that inclusions were more compliant than the matrix. Last, the contrast was set to a rather high value ($C = 20$), which was the case of highly rigid inclusions and very compliant matrix.

DVC analyses were run with different regularization lengths. For the first step, ℓ_{reg} was set to a high value (*i.e.,* 150 vx). Then, the displacement field at convergence was used to initialize the next step where the regularization length was decreased. This step-by-step (relaxation) process was continued until ℓ_{reg} reached 15 vx. In this study, too small ℓ_{reg} values (*i.e.,* less than twice the element size) were observed to be ineffective for mechanical regularization. When $C = 20$, DVC calculations with $\ell_{reg} < 30$ vx could not converge.

Figure 8(a) shows the displacement uncertainties and Figure 8(b) the maximum principal strain ϵ_1 uncertainties as functions of the regularization ℓ_{reg}. A decrease of ℓ_{reg} leads to an increase in displacement and strains fluctuations. This trend is consistent with the trade-off between spatial resolution (here controlled by the regularization length) and measurement uncertainty. Further, the more heterogeneous the regularization (*i.e.,* C departs from one), the higher the fluctuations since the regularization contrast increased (Equation (11)). On a more quantitative level, the strain uncertainty decay with ℓ_{reg} follows power laws that are not too far from -2.5, which are expected when the dominant source of uncer-

tainty corresponds to acquisition noise on the radiographs utilized to reconstruct 3D images [36].

Figure 8(c) shows the change of RMS residuals as functions of ℓ_{reg}. Their variation remained very limited since for any regularization length, the kinematics was very simple (essentially rigid body motions). These levels are baselines to which further analyses will be compared.

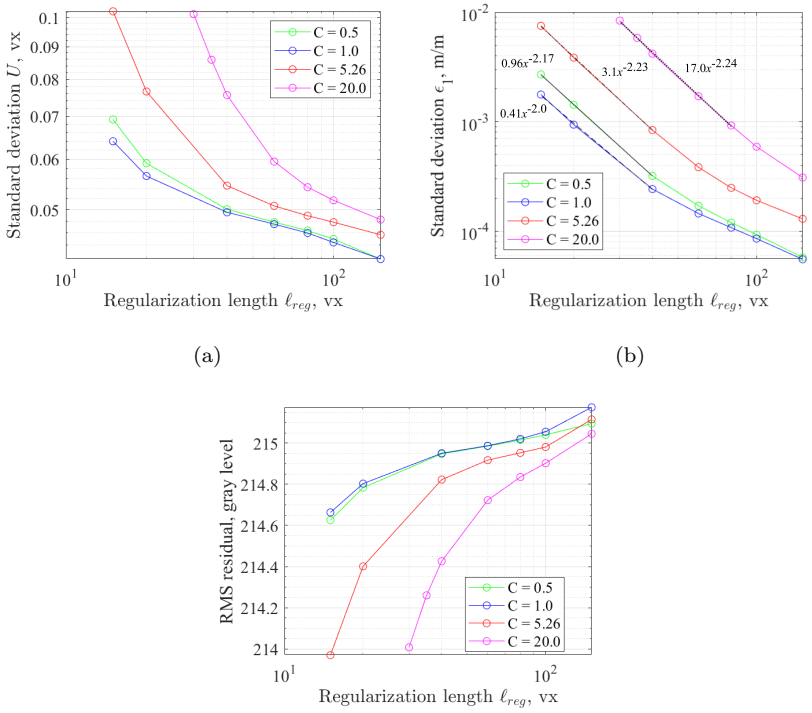

Fig. 8 (a) Displacement and (b) maximum principal strain uncertainties as functions of the regularization length for different contrasts. (c) Corresponding RMS residuals (note their small dynamic range)

3.3 DVC Analysis of Crack Propagation

The scan acquired right after specimen failure revealed that the crack had propagated on most of the ligament height. Therefore, DVC was run between the undeformed scan and this first scan. For the first DVC step, the regularization length was set to 100 vx, and gradually decreased down to 15 vx. The converged solution for higher ℓ_{reg} was used as initialization for the next step with less weight put on the mechanical part. The gradual relaxation of mechanical regularization allowed most of the long wave displacement components to be captured, and then iteratively converged to a better solution with short wave length fluctuations that were gradually restored. This iterative process was carried out for $C = 5.26$.

3D renderings of thresholded Lagrangian residual fields are shown in Figure 9. The maximum RMS level for $\ell_{reg} = 100$ vx was less than 1.4 times (287 gray level) the baseline RMS residual (215 gray level). The highest absolute levels correspond to the fractured surfaces, which were continuous and well defined. The absence of high residuals in the intact zones proves a good overall registration quality and efficient mechanical regularization of DVC. It is worth noting that when using the gray level residuals, the detection of the cracks was straightforward as all other heterogeneities, some of which had similar gray levels as the cracks, were no longer visible.

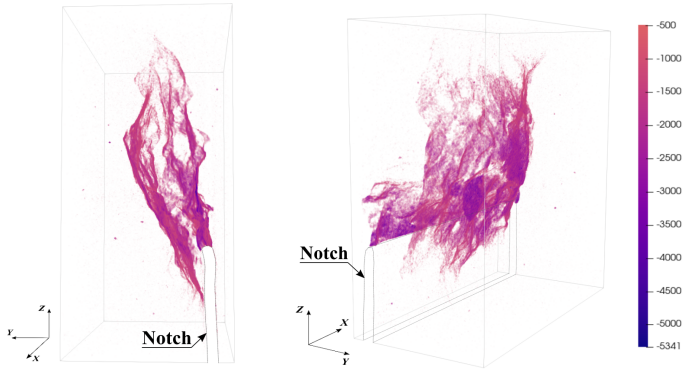

(a) (b)

Fig. 9 Thresholded Lagrangian residual field showing the fractured surfaces (ℓ_{reg} = 15 vx and $C = 5.26$). (a) Face and (b) side views

In terms of displacements, cracks induce discontinuities that mechanical regularization tends to spread over a zone whose size depends on ℓ_{reg} [47]. The followed relaxation procedure led to displacement jumps localized in a smaller domain. Consequently, the corresponding strains were higher and more concentrated (Figure 10).

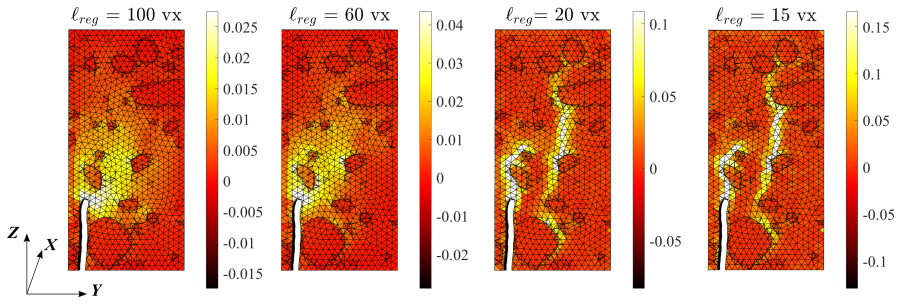

Fig. 10 Front face views of maximum principal strain ϵ_1 fields for different regularization lengths expressed in voxels ($C = 5.26$)

Figure 11(a) shows that the gray level residuals were essentially concentrated along the crack path. Very high maximum principal strains are observed in the zones where cracks were located. The differences in mechanical regularization performance in matrix and inclusions is visible in Figure 11(b). The crack crossed limestone aggregates (white in Figure 11(c)) where ℓ_{reg} was $\sqrt{C} = \sqrt{5.26} \approx 2.3$ times greater than in the matrix, which led to more diffuse strains with lower values.

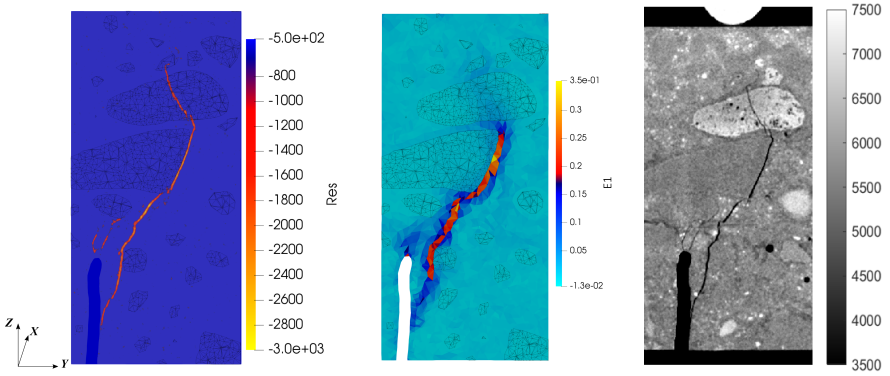

(a) (b) (c)

Fig. 11 Midsections of (a) gray level residuals ($\ell_{reg} = 15$ vx), (b) maximum principal strain ϵ_1, and (c) deformed volume

3.4 Contrast Influence

The relaxation process was also carried out for $C = 1.0$ (*i.e.,* homogeneous regularization), and the results are compared with the previous calculations. Figure 12(a) shows the RMS residual history during the relaxation process for the two considered contrasts. For $C > 1$, the RMS residuals were systematically lower, and dropped to 273 gray levels, while for $C = 1.0$ the minimum level was 279 gray levels. These levels are rather close to the baselines (*i.e.,* 214-5 gray levels). This

observation shows that the regularization used herein was not too strong and did not induce significant deviations.

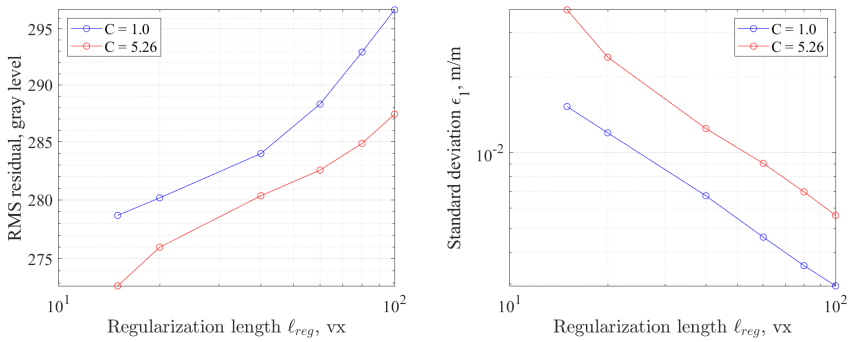

(a) (b)

Fig. 12 (a) RMS gray level residuals, and (b) maximum principal strain ϵ_1 fluctuations as functions of the regularization length ℓ_{reg} and contrast C

For the maximum principal strains (Figure 12(b)), their standard deviation was systematically larger for higher contrast, which allowed for more fluctuations especially at the interfaces between aggregates and the matrix to be captured. Moreover, the growth of strain fluctuations was more progressive for $C = 5.26$ along with the relaxation of mechanical regularization.

To further investigate the influence of contrast, the regularization length ℓ_{reg} was set to 20 vx, and the contrast C was varied between 0.5 and 20. The maximum principal strain fields (Figure 13) demonstrate how elastic contrast contributed to crack localization. The higher C, the less regularization was put on the matrix and the crack localized in fewer elements. In heterogeneous cementitious materials, the difference in mechanical properties of phases causes matrix-aggregate interfaces to

362 debond. This mechanism as well as damage in the matrix are better captured with
363 heterogeneous regularization.

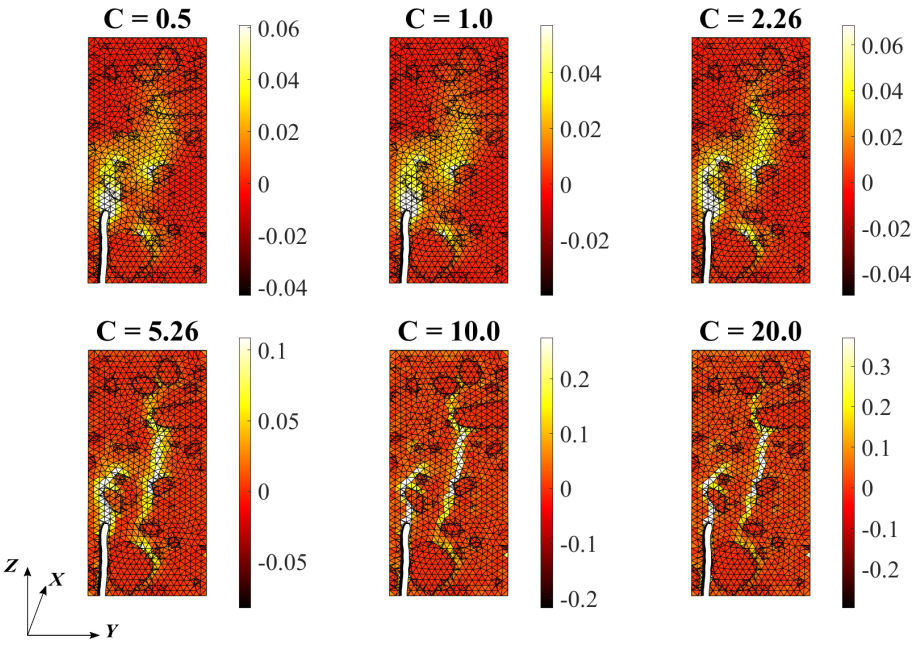

Fig. 13 Front face views of the maximum principal strain fields ϵ_1 for different contrasts ($\ell_{reg} = 20$ vx)

364 Figure 14(a) shows that higher contrasts resulted in lower residuals since they
365 allowed for more localized strains due to the presence of cracks. It is also reflected
366 in the increase of standard deviation of maximum principal strains (Figure 14(b)).
367 Although it may seem that taking a high value for C is a good option, the mean
368 of maximum principal strains grows as well with an increase of C. It is a signal
369 that too high contrasts result in "undeformed" aggregates and unphysical large
370 strains in the totality of the matrix. Therefore, taking a contrast value greater than
371 that based on physical properties of the constituents may result in displacement

fields that are no longer physically correct. Therefore, in further calculations the contrast was set to 5.26.

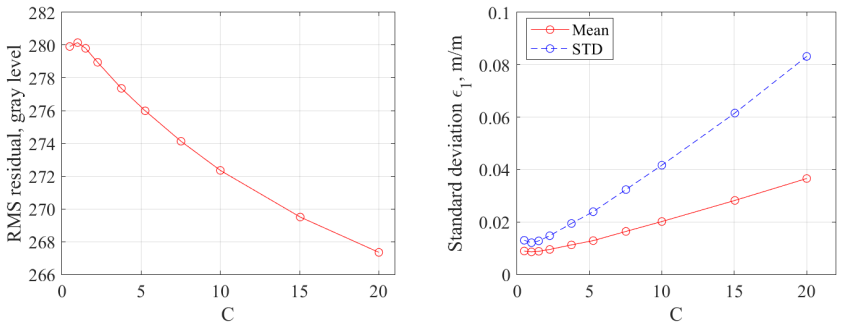

(a) (b)

Fig. 14 (a) Change of RMS residual with contrast and regularization length. (b) Mean and standard deviation of the maximum principal strains ϵ_1 as functions of contrast ($\ell_{reg} = 20$ vx)

4 Damage Quantification

After adding elastic contrast for heterogeneous mechanical regularization, the analysis was continued with the introduction of damage into mechanical regularization. A study of crack opening displacements and crack morphology at the mesoscale is finally proposed.

4.1 Damage Introduction into Mechanical Regularization

In the first stage, the heterogeneous regularization was taking into account the difference in mechanical behavior of different phases. In the present stage, damage can be considered in a similar manner [47]. The weight of mechanical regularization can be significantly reduced in the fractured zone, thereby allowing for large local strains. The damaged elements were selected based on two criteria, namely, the

385 average residual per element and Crack Opening Displacement (COD) $[\![u_I]\!]$, which
386 is estimated as

$$[\![u_I]\!] = \epsilon_1 \ \ell \tag{12}$$

387 by neglecting the regular contribution to mean strains [60]. To study the effect
388 of damage in mechanical regularization, two contrasts C were considered, namely,
389 1.0 and 5.26. The results of previous analyses with $\ell_{reg} = 20$ vx were chosen to
390 initialize calculations and select damaged elements. The thresholds and number of
391 selected damaged elements for both cases are listed in Table 4. For the gray level
392 residuals, the baseline levels were observed to be equal to 214-5 (Figure 8(a)).
393 Consequently, the thresholds were selected as about two times this level to avoid
394 false cracks. For the COD, their uncertainties were observed to be less than 0.1 vx
395 with the evaluated strain uncertainties (Figure 8(b)). Consequently, the threshold
396 COD for detecting damaged elements was set to 0.1 vx. The number of selected
397 damaged elements for the two contrasts were very close. It is concluded that the
398 selected criteria allowed for a reproducible description of the damaged zones. For
399 a higher contrast (*i.e.,* $C = 5.26$), the maximum principal strains in the damaged
400 zones were higher (Figure 13), and consequently the crack opening displacement.
401 The number of detected damaged elements was also slightly higher.

Table 4 Damaged element selection

Thresholds	$C = 1$	$C = 5.26$
RMS residual, gray level	400	
COD , vx	0.1	
Number of damaged elements	18,076	18,206

The detected damaged elements for $C = 5.26$ are presented in Figure 15. The damaged zone is continuous and replicates well the residual fields corresponding to fractured surfaces (Figure 9), thereby validating the choice of residual and COD criteria. The thickness of damaged zone consists of several elements since the mesh does not describe explicitly the fracture surface and, as a consequence, high residual values corresponding to the crack span over several elements in its vicinity.

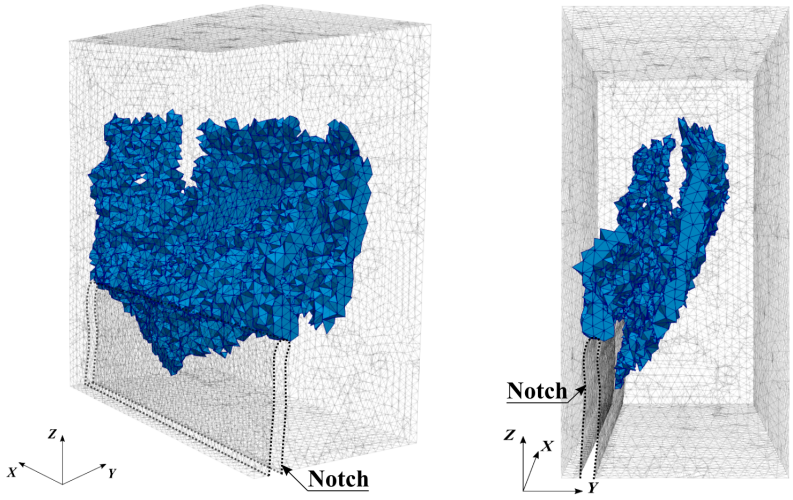

(a) (b)

Fig. 15 3D renderings of damaged elements (corresponding to cracks) in the mechanical regularization ($\ell_{reg} = 20$ vx, $C = 5.26$). (a) Side and (b) face views

Introducing a lower stiffness in damaged elements will help localize the inelastic strains due to cracks. Thus the weight of mechanical regularization in the remainder of the volume could be increased. In the following calculations, the regularization length was set to $\ell_{reg} = 60$ vx in order to increase the weight put on mechanical regularization in undamaged elements for which heterogeneous elastic-

ity is a very good approximation. Three different values were considered for the Young's modulus of the damaged elements E_d, namely, $0.2E_m$, $0.1E_m$ and $0.05E_m$. Figure 16 shows the maximum principal strain fields for different Young's moduli of damaged elements. Lower mechanical weight put in the damaged zones does allow for a better localization of strains in the cracked zones.

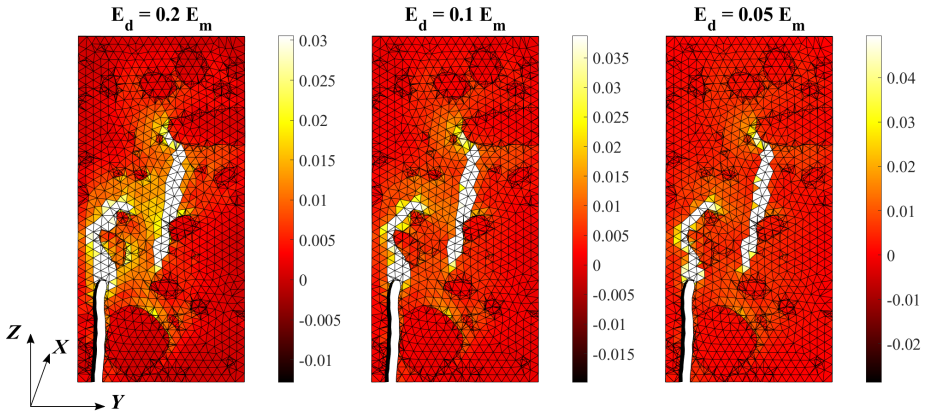

Fig. 16 Front face views of the maximum principal strain fields ϵ_1 for different elastic moduli of damaged elements ($\ell_{reg} = 60$ vx, $C = 5.26$)

Higher damage levels also led to lower global residuals (Figure 17), meaning convergence to a better solution, as well as higher strain fluctuations. Last, setting the damaged stiffness to values closer to zero (*i.e.,* $E_d < 0.05E_m$ in this study) resulted in the divergence of the DVC calculations. The elastic modulus of the damaged area E_d should be therefore set to the lowest possible value to allow for localized strains to occur, while retaining proper convergence of the DVC computations. Based on these results, in further calculations the Young's modulus of the damaged elements was set to 5% of the matrix modulus (*i.e.,* $E_d = 0.05\ E_m$).

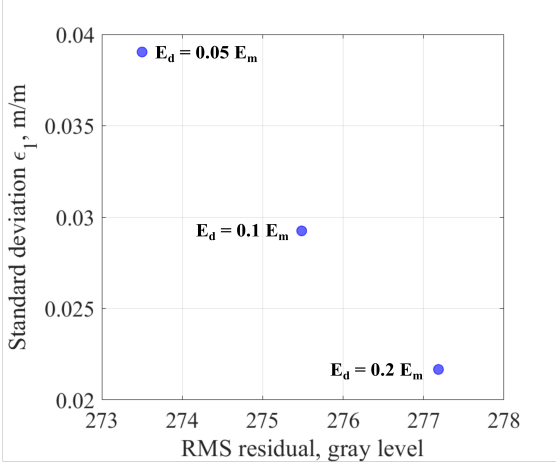

Fig. 17 Standard deviation of the maximum principal strain ϵ_1 compared to the RMS residual for different elastic moduli of damaged elements ($\ell_{reg} = 60$ vx, $C = 5.26$)

Figure 18 shows the maximum principal strain field for different contrasts and damage configurations. The introduction of damage into mechanical regularization was more effective for crack localization than the consideration of mechanical contrast between different phases (Figure 13). With the highest contrast, damage could also be better described at interfaces between the matrix and the aggregates.

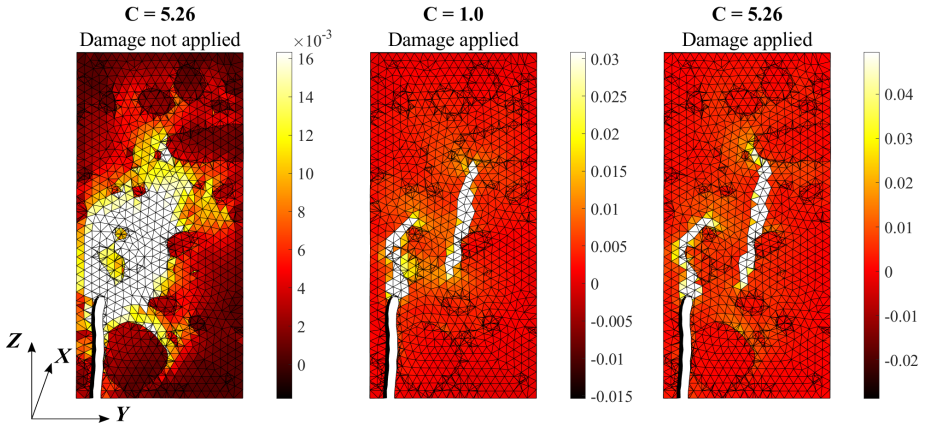

Fig. 18 Front face views of the maximum principal strain fields ϵ_1 for different contrasts and damage ($\ell_{reg} = 60$ vx)

Figure 19 displays the change of RMS residual and fluctuations of ϵ_1 fields characterized by their standard deviation. In terms of residual, the introduction of damage lowered their overall levels. The combination of both methods (*i.e.,* contrast and damage) gives a better solution in terms of residual levels and strain localization, which indicates a more correct description of the physical mechanisms. These results were kept for further damage quantification.

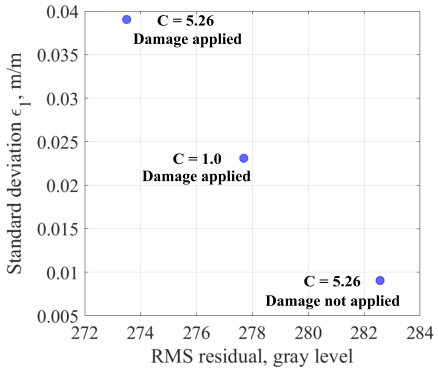

Fig. 19 Standard deviation of the maximum principal strain ϵ_1 compared to the RMS residual for different contrasts and damage implementations ($\ell_{reg} = 60$ vx)

4.2 Characterization of CODs

The dominant crack was observed to cross the cement paste matrix, aggregate-matrix interfaces and limestone aggregates. Once the DVC analysis was performed and the damaged elements detected, the damaged elements belonging to the matrix, interphases and aggregates were quantified (Figure 20). In cementitious materials, matrix-aggregate interfaces have different chemical compositions along with higher porosity. It is considered that due to the lower properties and mismatch of mechanical properties, damage initiates preferably in such interfacial zones, which lead to debonding [61]. Experimental evidence shows that the interfacial zone width varies in the 10-50 µm range [62, 63]. Since the average element size was ≈50 µm, the matrix elements adjacent to aggregates were considered as interphase elements for further analysis (Table 2).

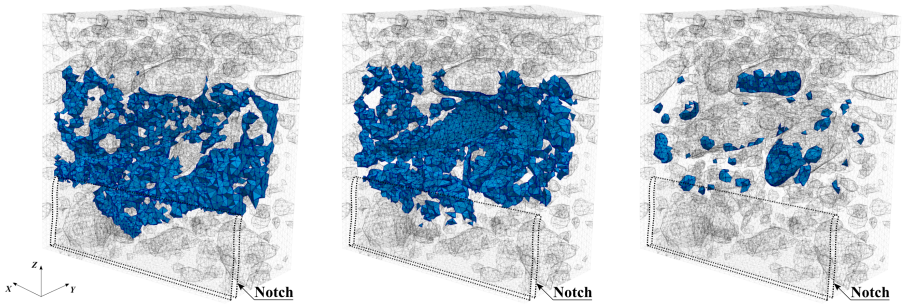

(a) (b) (c)

Fig. 20 Damaged elements belonging to (a) the matrix, (b) interphases, and (c) aggregates

The distribution of damaged zones between the three phases is reported in Table 5. The volume fraction of damaged elements was mostly in the matrix (>90%) with almost equal partitioning between interphases and matrix bulk. The maximum average COD is in interphases (7.3 µm), and the minimum is in the matrix bulk (6.2 µm). The highest COD fluctuations, which were characterized by their standard deviation, was in the aggregates (5.6 µm). For the other phases, the COD fluctuations were similar.

Table 5 Damaged zone characteristics

Parameters	Total	Bulk matrix	Interphases	Aggregates
Number of elements in damaged zone	18,206	8,340	8,329	1,537
Percentage of elements in damage zone	100%	46%	46%	8%
Damaged volume, mm^3	2.42	1.10	1.09	0.23
Average COD, µm	6.8	6.2	7.3	7.2
COD standard deviation, µm	4.6	4.2	4.7	5.6

The crack opening displacement was averaged over the total width of the sample and over its height with a 0.132 mm step. Figure 21(a) shows the COD field in

459 the specimen. Figure 21(b) reports the averaged crack opening displacement along
460 the specimen height for the entire crack, and Figure 21(c) for each individual phase.

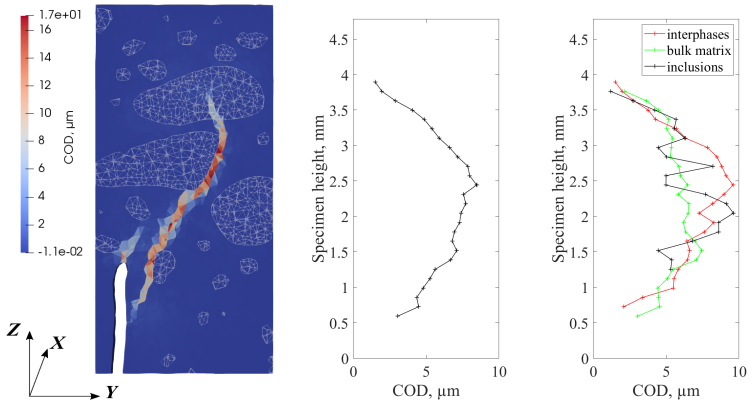

(a) (b) (c)

Fig. 21 (a) Cross-section (at $x = 2.5$ mm) of the COD field. (b) Average COD and (c) average COD per phase along the specimen height

461 The crack started below the notch root at 3.0 µm width and its opening in-
462 creased significantly up to 7.1 µm when it reached the notch root. Then the COD
463 grew slowly until it reached its maximum level of 8.5 µm at the mid-ligament
464 height, where a large aggregate with a vertical interface was located. Beyond the
465 mid-ligament, the COD decreased down to 1.5 µm at 3.9 mm specimen height. The
466 COD in the matrix bulk peaked at the notch root (7.4 µm) and then gradually
467 decreased as it propagated upward. The COD at interphases was higher than in
468 the matrix bulk over a significant part of the ligament with a maximum opening of
469 9.6 µm. The COD in aggregates was fluctuating considerably along the specimen
470 height. This effect was due to the relatively small number of cracked aggregates

and their sparse distribution in the volume (Figure 20(c)). However, locally the COD could reach 9.6 µm.

5 Conclusion and Perspectives

In the present study, an *in situ* three-point flexural test was carried out in an X-ray CT scanner on a small-scale mortar microbeam. A realistic 3D mesh was built consistently with the imaged underlying microstructure (based on a 5.3 µm resolution tomographic scan acquired prior to the *in situ* test). Mechanically regularized FE-DVC was adapted to heterogeneous materials by taking into account the difference between the elastic properties of the different phases of mortar. The introduction of elastic contrast C allowed the strain heterogeneities related to the underlying microstructure to be better described, and the inelastic strains to be better captured in the damaged zones. The contrast study showed that prescribing contrast levels above the expected properties of phases could result in unrealistic strains in the matrix. It is worth emphasizing that realistic Young's moduli of the various phases are needed to obtain trustworthy strain fields, especially when stronger mechanical regularization is enforced.

Furthermore, the damaged elements were selected based on previous computations for the introduction of damage in the regularization scheme. The Young's modulus in damaged elements was set to 5% of that in the undamaged matrix, which allowed displacement measurements to be more localized in the fractured zone. The estimation of crack opening displacements and crack morphology was carried out and gave more insight into the damage mechanisms at the mesoscale. The study thus demonstrated the potential of mechanically regularized FE-DVC

enriched with microstructure-based features for the quantification of damage at lower scales.

In future studies, the construction of 3D meshes consistent with fractured surfaces may improve the estimation of crack opening displacements [64, 65]. The test reported herein may also be used to calibrate numerical models accounting for the various damage mechanisms discussed herein.

Acknowledgements The work reported herein was carried out within the framework of the CEA-EDF-Framatome agreement.

Conflict of interest

The authors declare that they have no conflict of interest.

References

1. E. Maire and P. J. Withers. Quantitative x-ray tomography. *International Materials Reviews*, 59(1):1–43, 2014.
2. W. Trawiński, J. Tejchman, and J. Bobiński. A three-dimensional meso-scale modelling of concrete fracture, based on cohesive elements and x-ray µCT images. *Engineering Fracture Mechanics*, 189:27–50, 2018.
3. Z.-J. Yang, B.-B. Li, and J.-Y. Wu. X-ray computed tomography images based phase-field modeling of mesoscopic failure in concrete. *Engineering Fracture Mechanics*, 208:151–170, 2019.
4. S. T. Erdogan, P. N. Quiroga, D. W. Fowler, H. A. Saleh, R. A. Livingston, E. J. Garboczi, P. M. Ketcham, J. G. Hagedorn, and S. G. Satterfield. Three-dimensional shape analysis of coarse aggregates: New techniques for and preliminary results on several different coarse aggregates and reference rocks. *Cement and Concrete Research*, 36(9):1619–1627, 2006.

5. D. P. Bentz, Nicos S. Martys, P. Stutzman, M. S. Levenson, E. J. Garboczi, J. Dunsmuir, and L. M. Schwartz. X-ray microtomography of an astm c109 mortar exposed to sulfate attack. *MRS Online Proceedings Library (OPL)*, 370, 1994.
6. E. J. Garboczi and J. W. Bullard. Shape analysis of a reference cement. *Cement and Concrete Research*, 34(10):1933–1937, 2004.
7. E. J. Garboczi. Three-dimensional mathematical analysis of particle shape using x-ray tomography and spherical harmonics: Application to aggregates used in concrete. *Cement and Concrete Research*, 32(10):1621–1638, 2002.
8. H. He, Z. Guo, P. Stroeven, M. Stroeven, and L. J. Sluys. Strategy on simulation of arbitrary-shaped cement grains in concrete. *Image Analysis & Stereology*, 29(2):79–84, 2010.
9. E. Roubin, E. Andò, and S. Roux. The colours of concrete as seen by x-rays and neutrons. *Cement and Concrete Composites*, 104:103336, 2019.
10. D. P. Bentz, D. A. Quenard, H. M. Kunzel, J. Baruchel, F. Peyrin, N. S. Martys, and E. J. Garboczi. Microstructure and transport properties of porous building materials. II: Three-dimensional x-ray tomographic studies. *Materials and Structures*, 33(3):147–153, 2000.
11. K. Xu, A.S. Tremsin, J. Li, D.M. Ushizima, C.A. Davy, A. Bouterf, Y.T. Su, M. Marroccoli, A.M. Mauro, M. Osanna, A. Telesca, and P. J. M. Monteiro. Microstructure and water absorption of ancient concrete from pompeii: An integrated synchrotron microtomography and neutron radiography characterization. *Cement and Concrete Research*, 139:106282, 2021.
12. E. Gallucci, K. Scrivener, A. Groso, M. Stampanoni, and G. Margaritondo. 3d experimental investigation of the microstructure of cement pastes using synchrotron x-ray microtomography (µCT). *Cement and Concrete Research*, 37(3):360–368, 2007.
13. M. A. B. Promentilla, T. Sugiyama, T. Hitomi, and N. Takeda. Quantification of tortuosity in hardened cement pastes using synchrotron-based x-ray computed microtomography. *Cement and Concrete Research*, 39(6):548–557, 2009.
14. J. L. Provis, R. J. Myers, C. E. White, V. Rose, and J. S. J. van Deventer. X-ray microtomography shows pore structure and tortuosity in alkali-activated binders. *Cement and Concrete Research*, 42(6):855–864, 2012.

548 15. S. Lu, E. N. Landis, and D. T. Keane. X-ray microtomographic studies of pore structure
549 and permeability in portland cement concrete. *Materials and Structures*, 39(6):611–620,
550 2006.

551 16. D. P. Bentz. Three-dimensional computer simulation of portland cement hydration and
552 microstructure development. *Journal of the American Ceramic Society*, 80(1):3–21, 1997.

553 17. D. Bouvard, J. M. Chaix, R. Dendievel, A. Fazekas, J. M. Létang, G. Peix, and D. Que-
554 nard. Characterization and simulation of microstructure and properties of EPS lightweight
555 concrete. *Cement and Concrete Research*, 37(12):1666–1673, 2007.

556 18. O. Stamati, E. Roubin, E. Andò, and Y. Malecot. Tensile failure of micro-concrete:
557 from mechanical tests to FE meso-model with the help of x-ray tomography. *Meccanica*,
558 54(4):707–722, 2019.

559 19. T. T. Nguyen, J. Yvonnet, M. Bornert, and C. Chateau. Initiation and propagation of
560 complex 3d networks of cracks in heterogeneous quasi-brittle materials: direct comparison
561 between in situ testing-microCT experiments and phase field simulations. *Journal of the*
562 *Mechanics and Physics of Solids*, 95:320, 2016.

563 20. W. Ren, Z. Yang, R. Sharma, S. A. McDonald, and P. M. Mummery. Three-dimensional
564 in situ XCT characterisation and FE modelling of cracking in concrete. *Complexity*,
565 2018:e3856584, 2018.

566 21. F. Bernachy-Barbe and B. Bary. Effect of aggregate shapes on local fields in 3d mesoscale
567 simulations of the concrete creep behavior. *Finite Elements in Analysis and Design*,
568 156:13–23, 2019.

569 22. N. Burlion, D. Bernard, and D. Chen. X-ray microtomography: Application to microstruc-
570 ture analysis of a cementitious material during leaching process. *Cement and Concrete*
571 *Research*, 36(2):346–357, 2006.

572 23. T. Rougelot, N. Burlion, D. Bernard, and F. Skoczylas. About microcracking due to
573 leaching in cementitious composites: X-ray microtomography description and numerical
574 approach. *Cement and Concrete Research*, 40(2):271–283, 2010.

575 24. S. R Stock, N. K Naik, A. P Wilkinson, and K. E Kurtis. X-ray microtomography (mi-
576 croCT) of the progression of sulfate attack of cement paste. *Cement and Concrete Re-*
577 *search*, 32(10):1673–1675, 2002.

578 25. F. Bernachy-Barbe, T. Sayari, V. Dewynter-Marty, and V. L'Hostis. Using x-ray micro-
579 tomography to study the initiation of chloride-induced reinforcement corrosion in cracked
580 concrete. *Construction and Building Materials*, 259:119574, 2020.
581 26. B. Powierza, L. Stelzner, T. Oesch, C. Gollwitzer, F. Weise, and G. Bruno. Water migration
582 in one-side heated concrete: 4d in-situ CT monitoring of the moisture-clog-effect. *Journal*
583 *of Nondestructive Evaluation*, 38(1):15, 2018.
584 27. J. Y. Buffiere, E. Maire, J. Adrien, J. P. Masse, and E. Boller. In situ experiments with x
585 ray tomography: an attractive tool for experimental mechanics. *Experimental Mechanics*,
586 50(3):289–305, 2010.
587 28. E. N Landis, E. N Nagy, and D. T Keane. Microstructure and fracture in three dimensions.
588 *Engineering Fracture Mechanics*, 70(7):911–925, 2003.
589 29. E. Landis. X-ray tomography as a tool for micromechanical investigations of cement and
590 mortar. *Advances in X-ray Tomography for Geomaterials*, pages 79–93, 2010.
591 30. H. Elaqra, N. Godin, G. Peix, M. R'Mili, and G. Fantozzi. Damage evolution analysis in
592 mortar, during compressive loading using acoustic emission and x-ray tomography: Effects
593 of the sand/cement ratio. *Cement and Concrete Research*, 37(5):703–713, 2007.
594 31. R. C. K. Wong and K. T. Chau. Estimation of air void and aggregate spatial distributions
595 in concrete under uniaxial compression using computer tomography scanning. *Cement*
596 *and Concrete Research*, 35(8):1566–1576, 2005.
597 32. C. Poinard, E. Piotrowska, Y. Malecot, L. Daudeville, and E. N. Landis. Compression
598 triaxial behavior of concrete: the role of the mesostructure by analysis of x-ray tomographic
599 images. *European Journal of Environmental and Civil Engineering*, 16:s115–s136, 2012.
600 33. K. Wakimoto, J. Blunt, C. Carlos, P. J. M. Monteiro, C. P. Ostertag, and R. Albert. Digital
601 laminography assessment of the damage in concrete exposed to freezing temperatures.
602 *Cement and Concrete Research*, 38(10):1232–1245, 2008.
603 34. M. J. Mac, M. H. N. Yio, H. S. Wong, and N. R. Buenfeld. Analysis of autogenous
604 shrinkage-induced microcracks in concrete from 3d images. *Cement and Concrete Re-*
605 *search*, 144:106416, 2021.
606 35. B K Bay. Methods and applications of digital volume correlation. *The Journal of Strain*
607 *Analysis for Engineering Design*, 43(8):745–760, 2008.

608 36. A. Buljac, C. Jailin, A. Mendoza, J. Neggers, T. Taillandier-Thomas, A. Bouterf, B. Smani-
609 iotto, F. Hild, and S. Roux. Digital volume correlation: Review of progress and challenges.
610 *Experimental Mechanics*, 58(5):661–708, 2018.
611 37. B. K. Bay, T. S. Smith, D. P. Fyhrie, and M. Saad. Digital volume correlation: Three-
612 dimensional strain mapping using x-ray tomography. *Experimental Mechanics*, 39(3):217–
613 226, 1999.
614 38. S. Roux, F. Hild, P. Viot, and D. Bernard. Three dimensional image correlation from
615 x-ray computed tomography of solid foam. *Composites Part A: Applied Science and*
616 *Manufacturing*, 39(8):1253–1265, 2008.
617 39. N. Ducoulombier, C. Chateau, M. Bornert, J.-F. Caron, P. Aimedieu, T. Weitkamp, J. Per-
618 rin, A. King, and M. Scheel. X-ray tomographic observations of microcracking patterns
619 in fibre-reinforced mortar during tension stiffening tests. *Strain*, 56(6):e12347, 2020.
620 40. S. Hong, P. Liu, J. Zhang, C. Kuang, B. Dong, Q. Luo, and W. Liu. Interior fracture
621 analysis of rubber-cement composites based on x-ray computed tomography and digital
622 volume correlation. *Construction and Building Materials*, 259:119833, 2020.
623 41. R. Lorenzoni, I. Curosu, F. Léonard, S. Paciornik, V. Mechtcherine, F. A. Silva, and
624 G. Bruno. Combined mechanical and 3d-microstructural analysis of strain-hardening
625 cement-based composites (SHCC) by in-situ x-ray microtomography. *Cement and Con-*
626 *crete Research*, 136:106139, 2020.
627 42. L. Mao, Z. Yuan, M. Yang, H. Liu, and Fu-pen Chiang. 3d strain evolution in concrete using
628 in situ x-ray computed tomography testing and digital volumetric speckle photography.
629 *Measurement*, 133:456–467, 2019.
630 43. M. Mostafavi, N. Baimpas, E. Tarleton, R. C. Atwood, S. A. McDonald, A. M. Korsunsky,
631 and T. J. Marrow. Three-dimensional crack observation, quantification and simulation in
632 a quasi-brittle material. *Acta Materialia*, 61(16):6276–6289, 2013.
633 44. F. Bennai, C. El Hachem, K. Abahri, and R. Belarbi. Microscopic hydric characterization
634 of hemp concrete by x-ray microtomography and digital volume correlation. *Construction*
635 *and Building Materials*, 188:983–994, 2018.
636 45. E. A. Chavez Panduro, B. Cordonnier, K. Gawel, I. Børve, J. Iyer, S. A. Carroll, L. Michels,
637 M. Rogowska, J. A. McBeck, H. O. Sørensen, S. D. C. Walsh, F. Renard, A. Gibaud,

638 M. Torsæter, and D. W. Breiby. Real time 3d observations of portland cement carbonation
639 at CO2 storage conditions. *Environmental Science & Technology*, 54(13):8323–8332, 2020.
640 46. H. Jiang, H. Ji, N. Jin, Y. Tian, X. Jin, H. Ye, D. Yan, and Z. Tian. Simulation and ex-
641 perimental verification of the non-uniform corrosion cracking process of reinforced mortar
642 specimen. *Construction and Building Materials*, 265:120522, 2020.
643 47. F. Hild, A. Bouterf, and S. Roux. Damage measurements via DIC. *International Journal*
644 *of Fracture*, 191(1):77–105, 2015.
645 48. F. Hild, A. Fanget, J. Adrien, E. Maire, and S. Roux. Three-dimensional analysis of
646 a tensile test on a propellant with digital volume correlation. *Archives of Mechanics*,
647 63(5):1–20, 2011.
648 49. F. Hild, S. Roux, D. Bernard, G. Hauss, and M. Rebai. On the use of 3d images and
649 3d displacement measurements for the analysis of damage mechanisms in concrete-like
650 materials. In *VIII International Conference on Fracture Mechanics of Concrete and*
651 *Concrete Structures FraMCoS-8*, 2013.
652 50. C. Chateau, T. T. Nguyen, M. Bornert, and J. Yvonnet. DVC-based image subtraction
653 to detect microcracking in lightweight concrete. *Strain*, 54(5):e12276, 2018.
654 51. H. Leclerc, J.-N. Périé, S. Roux, and F. Hild. Voxel-scale digital volume correlation.
655 *Experimental Mechanics*, 51(4):479–490, 2011.
656 52. T. Taillandier-Thomas, S. Roux, T. F. Morgeneyer, and F. Hild. Localized strain field
657 measurement on laminography data with mechanical regularization. *Nuclear Instruments*
658 *and Methods in Physics Research Section B: Beam Interactions with Materials and Atoms*,
659 324:70–79, 2014.
660 53. R. Naylor, F. Hild, C. Fagiano, M. Hirsekorn, Y. Renollet, B. Tranquart, and E. Baranger.
661 Mechanically regularized FE DIC for heterogeneous materials. *Experimental Mechanics*,
662 59(8):1159–1170, 2019.
663 54. F. Hild and S. Roux. Digital image correlation. In K. Rastogi Pramod and Hack Er-
664 win, editors, *Optical Methods for Solid Mechanics. A Full-Field Approach*, pages 183–228.
665 Wiley-VCH.
666 55. H. Leclerc, J.N. Périé, F. Hild, and S. Roux. Digital volume correlation: What are the
667 limits to the spatial resolution? *Mechanics & Industry*, 13:361–371, 2012.

668 56. A. Mendoza, J. Neggers, F. Hild, and S. Roux. Complete mechanical regularization applied
669 to digital image and volume correlation. *Computer Methods in Applied Mechanics and*
670 *Engineering*, 355:27–43, 2019.
671 57. H. Leclerc, J. Neggers, F. Mathieu, F. Hild, and S. Roux. Correli 3.0. Agence pour la
672 Protection des Programmes, Paris (France). IDDN.FR.001.520008.000.S.P.2015.000.31500,
673 2015.
674 58. P. Auger, T. Lavigne, B. Smaniotto, M. Spagnuolo, F. dell'isola, and F. Hild. Poynting
675 effects in pantographic metamaterial captured via multiscale DVC. *Journal of Strain*
676 *Analysis for Engineering Design*, 56(7):462–477, 2021.
677 59. A. Tsitova, F. Bernachy-Barbe, B. Bary, and F. Hild. In-situ x-CT test on mortar micro-
678 specimen coupled with mesoscale numerical simulations of fracture. In F. Kanavaris,
679 F. Benboudjema, and M. Azenha, editors, *International RILEM Conference on Early-Age*
680 *and Long-Term Cracking in RC Structures*, RILEM Bookseries, pages 239–251. Springer
681 International Publishing, 2021.
682 60. A.A. Vakulenko and M.L. Kachanov. Continuum theory of medium with cracks. *Isv. AN*
683 *SSSR, Mekh. Tverdogo Tela*, 4:159–166, 1971.
684 61. J. P. Ollivier, J. C. Maso, and B. Bourdette. Interfacial transition zone in concrete.
685 *Advanced Cement Based Materials*, 2(1):30–38, January 1995.
686 62. K. L. Scrivener, A. K. Crumbie, and P. Laugesen. The interfacial transition zone (ITZ)
687 between cement paste and aggregate in concrete. *Interface Science*, 12(4):411–421, 2004.
688 63. P. Mondal, S. P. Shah, and L. D. Marks. Nanomechanical properties of interfacial transition
689 zone in concrete. In Z. Bittnar, P. J. M. Bartos, J. Němeček, V. Šmilauer, and J. Zeman,
690 editors, *Nanotechnology in Construction 3*, pages 315–320. Springer, 2009.
691 64. J. Réthoré, J.P. Tinnes, S. Roux, J.Y. Buffière, and F. Hild. Extended three-dimensional
692 digital image correlation (X3D-DIC). *Comptes Rendus Mécanique*, 336:643–649, 2008.
693 65. J. Rannou, N. Limodin, J. Réthoré, A. Gravouil, W. Ludwig, M.C. Baïetto, J.Y. Buffière,
694 A. Combescure, F. Hild, and S. Roux. Three dimensional experimental and numerical
695 multiscale analysis of a fatigue crack. *Computer Methods in Applied Mechanics and En-*
696 *gineering*, 199:1307–1325, 2010.